





Cite this: *Phys. Chem. Chem. Phys.*,  
2025, 27, 6656

# An environmentally adaptive gold single-atom catalyst with variable valence states†

Meiliang Ma,‡ Wen Liu,‡ Xiaojuan Hu,\* Ying Jiang, Wentao Yuan,  
Zhong-Kang Han \* and Yong Wang 

Single-atom catalysts revolutionize catalysis by maximizing atomic efficiency and enhancing reaction specificity, offering high activity and selectivity with minimal material usage, which is crucial for sustainable processes. However, the unique properties that distinguish single-atom catalysts from other forms, including bulk and nanoparticle catalysts, as well as the physical mechanisms behind their high activity and selectivity, remain unclear, limiting their broader application. Here, through first-principles calculations, we have identified an environmentally adaptive gold single-atom catalyst on a CeO<sub>2</sub>(111) surface capable of adjusting its valence state in response to different environmental conditions. This adaptability enables the catalyst to simultaneously maintain high stability and activity. In a CO gas atmosphere, numerous oxygen vacancies form on the CeO<sub>2</sub>(111) surface, where Au single atoms stably adsorb, exhibiting a negative oxidation state that deactivates the catalyst. In an O<sub>2</sub> atmosphere, these vacancies are filled, causing the Au single atoms to adsorb onto lattice oxygen and become oxidized to a positive oxidation state, thereby reactivating the catalyst. Under CO oxidation reaction conditions, the Au single atoms oscillate between these positive and negative oxidation states, effectively facilitating the CO oxidation process. These findings provide new insights into the unique properties and high performance of single-atom catalysts, contributing to a better understanding and utilization of these catalysts in various applications.

Received 5th February 2025,  
Accepted 28th February 2025

DOI: 10.1039/d5cp00468c

rsc.li/pccp

## Introduction

Since Zhang *et al.*<sup>1</sup> successfully prepared Pt single-atom catalysts supported on FeO<sub>x</sub> using a co-precipitation method in 2011, single-atom catalysts (SACs) have gained significant attention. These catalysts feature isolated single atoms as active centers, uniformly dispersed and anchored on various supports.<sup>2</sup> Due to their exceptional properties, such as high activity and selectivity, SACs are widely applied in diverse catalytic reactions including CO oxidation,<sup>1,3–7</sup> CO<sub>2</sub> reduction,<sup>8–18</sup> and water-gas shift reactions.<sup>19–27</sup> For example, Liu *et al.*<sup>28</sup> employed a straightforward photochemical method to prepare a stable Pd/TiO<sub>2</sub> SAC at room temperature, which demonstrated high activity and stability in hydrogenation reactions. Xie *et al.*<sup>29</sup> reported an atomically dispersed Co and N co-doped carbon (Co–N–C) catalyst that exhibited oxygen reduction reaction activity comparable to an Fe–N–C catalyst but with four-fold greater durability. Moreover, Kyriakou *et al.*,<sup>30</sup> through desorption measurements and

high-resolution scanning tunneling microscopy, found that isolated Pd atoms on a Cu surface significantly reduced the energy barriers for hydrogen adsorption and desorption, facilitating selective hydrogenation of styrene and acetylene, which is not achievable with pure Cu or Pd metals. While these studies have advanced our understanding of SACs, key mechanistic aspects—particularly those involving dynamic interactions between single atoms, supports, and reaction environments—have not yet been fully resolved.

First-principles calculations are crucial for elucidating the reaction mechanisms of SACs. For example, Tong *et al.*<sup>31</sup> used density functional theory (DFT) to investigate the efficient oxygen reduction reaction (ORR) mechanism of a bimetallic SAC consisting of Cu and Zn on a nitrogen-doped carbon support. They found that the influence of Zn on the Cu's d-orbital electron distribution facilitates the stretching and cleavage of O–O bonds at the Cu active site, thus accelerating the rate-determining step involving OOH\*. Similarly, DFT studies by Riley *et al.*<sup>32</sup> proposed a mechanism for the selective hydrogenation of alkynes catalyzed by ceria, which involves the heterolytic dissociation of H<sub>2</sub> at oxygen vacancies on CeO<sub>2</sub>(111), facilitated by a suppressed Lewis pair composed of spatially separated O and Ce sites. Based on this mechanism, they suggested using Ni-doped ceria to generate oxygen vacancies,

Center of Electron Microscopy, School of Materials Science and Engineering,  
Zhejiang University, Hangzhou, 310027, China. E-mail: xiaojuanhu@zju.edu.cn,  
hankz@zju.edu.cn

† Electronic supplementary information (ESI) available. See DOI: <https://doi.org/10.1039/d5cp00468c>

‡ Denotes equal contributions.



a principle that was confirmed experimentally to enhance activity in the selective hydrogenation of acetylene. However, SACs are inherently complex systems. To stabilize single atoms, substrates that can be reduced, such as  $\text{CeO}_2$ , are typically used. This can lead to multiple oxidation states of the single atoms, the presence of oxygen vacancies, and redox processes involving substrate metal atoms. For example, in the Au- $\text{CeO}_2$  SAC, Au atoms can exist in different oxidation states and  $\text{CeO}_2$  is reducible, exhibiting oxygen vacancies along with transformations between  $\text{Ce}^{4+}$  and  $\text{Ce}^{3+}$  ions. These dynamic interactions complicate the precise control and mechanistic interpretation of SAC behavior under operando conditions. For instance, theoretical calculations by Camellone *et al.*<sup>33</sup> suggested that, in a CO atmosphere, Au atoms positioned above the oxygen vacancies of ceria adopt a negative charge state, thus losing the ability to activate CO further. In contrast, experimental X-ray photoelectron spectroscopy (XPS) studies by Guo *et al.*<sup>34</sup> reported that single Au atoms exhibit a high oxidation state with notable activity, a finding that conflicts with theoretical results. This high oxidation state is not explained by Au doping at Ce sites, as calculations indicate that such doping is energetically unfavorable.<sup>35,36</sup> Such discrepancies highlight the need for deeper insights into how environmental adaptability governs SAC performance.

In this study, we conducted a detailed examination of the thermodynamic and kinetic behaviors of single-atom Au catalysts under CO,  $\text{O}_2$ , and CO oxidation reaction conditions using first-principles calculations. We discovered an environmentally adaptive gold SAC on the  $\text{CeO}_2(111)$  surface, which uniquely adjusts its valence state in response to varying environmental conditions. Furthermore, by contrasting the performance of the single-atom  $\text{Au}_1$  catalyst with larger  $\text{Au}_4$  and  $\text{Au}_{10}$  catalyst systems, we underscored the distinctive ability of single-atom catalysts to efficiently modulate their valence states, enabling them to maintain both high stability and activity simultaneously.

## Computational details

All electronic structure calculations were performed using density functional theory. Valence electron densities were expanded using plane-wave basis sets, and the projected augmented-wave (PAW) method<sup>37</sup> was used to describe the interactions between the core and the valence electrons. We conducted these calculations using the Vienna ab initio simulation package (VASP 5.4.4).<sup>38</sup> The spin-polarized Kohn–Sham calculations were based on the generalized gradient approximation, employing the Perdew–Burke–Ernzerhof (PBE)<sup>39</sup> exchange–correlation functional. Additionally, the Hubbard-type on-site Coulomb interaction term (PBE+ $U$ ), according to Dudarev's approximation, was applied to the f-electrons of Ce atoms<sup>40,41</sup> with a Hubbard  $U$  value set at 5.0 eV to describe the localization of excess charges in Ce 4f states, consistent with studies recommending  $U$  values in the range of 4.5–6.0 eV.<sup>40,42,43</sup> In all these calculations, we applied the projector augmented-wave<sup>44</sup> method and an energy cut-off of 400 eV.

The  $\text{CeO}_2$  support was modeled using a  $4 \times 4$  supercell comprising a nine-layer slab with a 15 Å vacuum space to avoid

interactions between periodic images. The bottom three layers (O–Ce–O) were fixed at their bulk positions, while the remaining layers were allowed to relax during geometry optimization. The force convergence criterion was set at 0.05 eV Å<sup>−1</sup>. A gamma-centered  $1 \times 1 \times 1$  k-point mesh was used for the Brillouin zone integration. Testing a  $2 \times 2 \times 1$  k-point mesh for the  $(4 \times 4)$   $\text{CeO}_2$  supercell revealed only minor variations (approximately 10 meV) in CO adsorption energy, confirming the convergence of our gamma-point calculations. The transition states were located using the climbing-image nudged elastic band<sup>45,46</sup> and dimer methods.<sup>47</sup> The adsorption energies were calculated using the following equation:

$$E_{\text{ad}} = E_{\text{mol/surf}} - (E_{\text{surf}} + E_{\text{mol}}) \quad (1)$$

where  $E_{\text{mol/surf}}$  is the total energy of the surface with the adsorbed molecules,  $E_{\text{surf}}$  is the energy of the substrate, and  $E_{\text{mol}}$  is the energy of the isolated molecules in the gas phase.

## Results and discussion

### Deactivation of the Au single atom in the CO atmosphere

To determine the most stable configuration of the  $\text{Au}_1$  atom on the  $\text{CeO}_2(111)$  surface, different high-symmetry adsorption sites were considered (Fig. S1, ESI†). The most energetically favorable configuration was found when the Au atom adsorbed at the bridge site of surface oxygen, with an adsorption energy of −1.41 eV, aligning with previous literature.<sup>33</sup> This configuration also exhibited a +1 oxidation state for the Au atom, corroborated by spin charge density analysis which revealed the presence of one  $\text{Ce}^{3+}$  ion, indicating electron transfer from Au to the substrate (Fig. S2, ESI†). In the CO atmosphere, the exceptional oxygen buffering capacity of  $\text{CeO}_2$  enables CO oxidation through interaction with lattice oxygen, forming  $\text{CO}_2$  and creating an oxygen vacancy. The Au atom strongly interacts with this newly formed vacancy, positioning itself above it as shown in Fig. 1a. The Au atom is positioned 1.21 Å above the oxygen vacancy, with an Au–Ce bond length of 3.12 Å, aligning with reported results.<sup>33</sup> Calculations indicate that while aggregation of negatively charged Au atoms into clusters is thermodynamically feasible, a high kinetic barrier (approximately 1.2 eV) effectively prevents such aggregation under typical experimental conditions. Bader charge analysis reveals a net charge of −0.29  $e$  for the Au atom, classifying it as  $\text{Au}^{\delta-}$ . We also tested other charge calculation methods, which showed a minimal effect on the charge distribution trends. Differential charge density analysis (Fig. 1b) shows electron accumulation at the Au atom, confirming the negatively charged nature of  $\text{Au}^{\delta-}$ . The removal of one lattice oxygen results in the generation of two excess electrons localized at the cerium site, which reduce two  $\text{Ce}^{4+}$  to  $\text{Ce}^{3+}$  ions. For  $\text{Au}_1$  adsorbed on the  $\text{CeO}_2(111)$  system with one oxygen vacancy [ $\text{Au}_1@ \text{CeO}_2(111)\text{-O}_v$ ], the presence of one  $\text{Ce}^{3+}$  ion was observed from the spin charge density analysis, indicating an oxidation state of −1 for Au. Additionally, we assessed the impact of  $\text{Ce}^{3+}$  ions positioning on the energy of various structures during



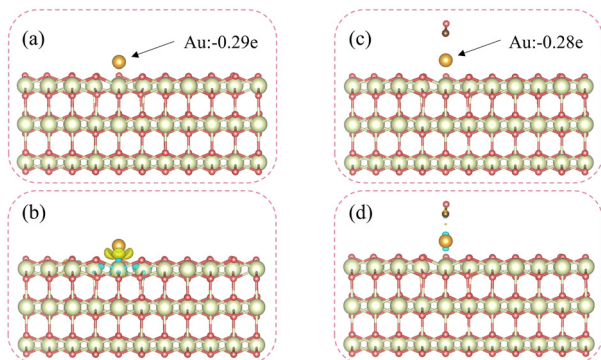


**Fig. 1** Configuration and electronic structure analysis of  $\text{Au}_1@ \text{CeO}_2(111)\text{-O}_\text{v}$ . (a) System configuration and Bader charge of the  $\text{Au}_1$  atom. (b) Differential charge density between  $\text{Au}_1$  and  $\text{CeO}_2(111)\text{-O}_\text{v}$ , and an isosurface displayed at  $0.01 \text{ e } \text{\AA}^{-3}$ . (c) System configuration with adsorbed CO and Bader charge of the  $\text{Au}_1$  atom. (d) Differential charge density between CO and the  $\text{Au}_1@ \text{CeO}_2(111)\text{-O}_\text{v}$  system, and an isosurface displayed at  $0.01 \text{ e } \text{\AA}^{-3}$ .

these processes, finding that the position of  $\text{Ce}^{3+}$  does not affect the overall reaction energy (Fig. S2–S5, ESI†).

We positioned a CO molecule above the Au atom to evaluate the CO adsorption capacity of  $\text{Au}^{\delta-}$ , resulting in the configuration shown in Fig. 1c. The Au–C bond length measures  $2.27 \text{ \AA}$ , and the C–O bond length remains at  $1.15 \text{ \AA}$ , identical to that in a free CO molecule. The adsorption energy of CO on  $\text{Au}^{\delta-}$  is approximately zero, which is significantly higher than the  $-2.54 \text{ eV}$  calculated for CO adsorption on an Au atom on the stoichiometric  $\text{CeO}_2(111)$  surface. This indicates that  $\text{Au}^{\delta-}$  possesses negligible CO adsorption capacity. Although the thermodynamic energy for CO to displace the Au atom is about  $1.36 \text{ eV}$  lower than that of the Au atom remaining at the vacancy, a substantial kinetic barrier of around  $1 \text{ eV}$  hinders this displacement, particularly at lower temperatures, suggesting that CO is unlikely to displace the Au atom from the vacancy site under typical reaction conditions. Bader charge analysis of this configuration shows a net charge of  $-0.28 e$  on the Au atom, nearly unchanged from the pre-adsorption state, confirming the persistence of the  $\text{Au}^{\delta-}$  state. The differential charge density (Fig. 1d) illustrates minimal charge transfer between the CO molecule and  $\text{Au}_1@ \text{CeO}_2(111)\text{-O}_\text{v}$ . This minimal charge transfer and the Bader charge analysis collectively demonstrate that  $\text{Au}^{\delta-}$ , in the presence of an oxygen vacancy, lacks the capacity to adsorb and activate CO. This finding is consistent with previous calculations.<sup>33</sup> However, experimental evidence suggests the existence of high-valence-states and highly active Au single atoms,<sup>34</sup> which contradicts these theoretical calculations. We propose that the discrepancy may arise from the interactions of the  $\text{Au}_1@ \text{CeO}_2(111)\text{-O}_\text{v}$  system with oxygen molecules.

### Reactivation of Au single atoms in the $\text{O}_2$ atmosphere

In the Mars–van Krevelen (MvK) mechanism, the catalyst undergoes reduction by forming oxygen vacancies during the initial oxidation step. For subsequent oxidation reactions, dissociatively adsorbed oxygen is needed to fill these vacancies and reoxidize the catalyst. To determine if the  $\text{Au}_1@ \text{CeO}_2(111)\text{-O}_\text{v}$  catalyst follows

this mechanism for CO oxidation in an oxygen atmosphere and thus reactivates the deactivated  $\text{Au}_1@ \text{CeO}_2(111)\text{-O}_\text{v}$ , we evaluated the potential for molecular oxygen to fill the surface oxygen vacancies. This process would transition the  $\text{Au}^{\delta-}$  state to  $\text{Au}^{\delta+}$ , thereby restoring the catalyst's ability to oxidize CO effectively.

As shown in Fig. 2a, molecular oxygen from the atmosphere overcomes a low energy barrier ( $0.34 \text{ eV}$ ) to fill the oxygen vacancy beneath the deactivated  $\text{Au}^{\delta-}$  atom (Fig. S6, ESI†), with an adsorption energy of  $-1.39 \text{ eV}$ . Additionally, our calculations indicate that CO does not occupy the oxygen vacancy, further supporting the proposed mechanism (Fig. S7, ESI†). One oxygen atom from the  $\text{O}_2$  molecule occupies the vacancy, while the other forms a bond with lattice oxygen, resulting in an O–O bond length of  $1.48 \text{ \AA}$ , which is longer than the  $1.23 \text{ \AA}$  bond length in a free  $\text{O}_2$  molecule. Bader charge analysis indicates that the Au atom acquires a  $+1 e$  charge, suggesting substantial charge transfer between the Au atom and the substrate, induced by the adsorbed  $\text{O}_2$ . Differential charge density analysis (Fig. 2b) confirms this significant charge transfer. This transformation reactivates the  $\text{Au}_1@ \text{CeO}_2(111)\text{-O}_\text{v}$  catalyst for CO oxidation. To confirm the catalytic capability of the reactivated  $\text{Au}_1@ \text{CeO}_2(111)\text{-O}_\text{v}\text{-O}_2$  structure, we calculated the adsorption of a CO molecule and identified the most stable configuration, as shown in Fig. 2c. After CO adsorption, the bond length between the original peroxide oxygen and the Au atom elongates from  $2.07 \text{ \AA}$  to  $3.18 \text{ \AA}$ , while the bond length between the Au atom and the lattice oxygen shortens from  $2.05 \text{ \AA}$  to  $1.96 \text{ \AA}$ . The bond length between C and Au measures  $1.87 \text{ \AA}$ , and the C–O bond length extends slightly to  $1.15 \text{ \AA}$  from  $1.14 \text{ \AA}$  in a free CO molecule. The adsorption energy of CO on this activated structure is  $-1.68 \text{ eV}$ . Bader charge analysis shows a  $+0.73 e$  charge on the Au atom, indicating that in both structures (Fig. 2a and c), Au is positively charged and thus catalytically active for CO oxidation. Differential charge density analysis (Fig. 2d) demonstrates obvious charge transfer between the CO molecule and the  $\text{Au}_1@ \text{CeO}_2(111)\text{-O}_\text{v}\text{-O}_2$  catalyst, confirming the catalyst's capability to oxidize CO effectively. Additionally, our calculations

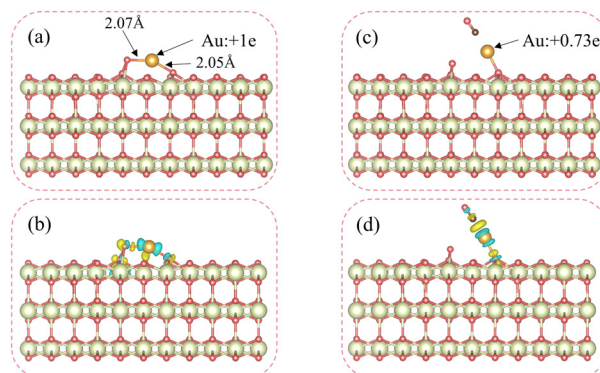


**Fig. 2** Configuration and electronic structure analysis of  $\text{Au}_1@ \text{CeO}_2(111)\text{-O}_\text{v}\text{-O}_2$ . (a) Configuration of  $\text{Au}_1@ \text{CeO}_2(111)\text{-O}_\text{v}\text{-O}_2$  and Bader charge of the  $\text{Au}_1$  atom. (b) Differential charge density between  $\text{Au}_1$  and  $\text{CeO}_2(111)\text{-O}_\text{v}\text{-O}_2$ , and an isosurface displayed at  $0.01 \text{ e } \text{\AA}^{-3}$ . (c) Configuration of  $\text{Au}_1@ \text{CeO}_2(111)\text{-O}_\text{v}\text{-O}_2$  with the adsorbed CO molecule and Bader charge of the  $\text{Au}_1$  atom. (d) Differential charge density between CO and the  $\text{Au}_1@ \text{CeO}_2(111)\text{-O}_\text{v}\text{-O}_2$  system, and an isosurface displayed at  $0.01 \text{ e } \text{\AA}^{-3}$ .





indicate that the attempt to adsorb a second CO molecule on  $\text{Au}_1@ \text{CeO}_2(111)$  leads to an increased distance of 3.44 Å from the Au atom, which is significantly larger than the typical CO adsorption distance (Fig. S8, ESI†). This suggests that further CO adsorption is energetically unfavorable in this configuration.

Through analyses including the Bader charge and differential charge density, we have shown that the  $\text{Au}^{\delta-}$  state on an oxygen vacancy lacks the capacity to adsorb and activate CO, consistent with previous findings.<sup>33</sup> However, the introduction of molecular oxygen into the oxygen vacancy transforms  $\text{Au}^{\delta-}$  into  $\text{Au}^{\delta+}$ , effectively reactivating the  $\text{Au}_1@ \text{CeO}_2(111)\text{-O}_V$  catalyst for CO oxidation. This reactivation mechanism conforms to the MvK mechanism and offers new insights into the behavior of the  $\text{Au}_1@ \text{CeO}_2(111)$  SAC.

### Valence state oscillations of the environmentally adaptive gold single-atom catalyst under CO oxidation reaction conditions

To further elucidate the deactivation and reactivation mechanisms of the  $\text{Au}_1@ \text{CeO}_2(111)$  catalyst, we primarily focused on Au atoms adsorbed on three specific sites: the bridge site of surface oxygen ( $\text{B}_O$ ), the top site of the surface oxygen vacancy ( $\text{O}_V$ ), and the site where the oxygen vacancy is filled by an  $\text{O}_2$  molecule ( $\text{O}_V\text{-O}_2$ ) (Fig. 3(a)). We conducted a projected density of states (PDOS) analysis of Au atoms at these three distinct sites (Fig. 3b).

The PDOS for the Au atom on  $\text{O}_V$  shows orbitals located farther from the Fermi level, suggesting a more stable electronic state that is less reactive with other atoms. This stability is also

**Table 1** The Bader charges and CO adsorption energies for Au atoms on different sites

Adsorption site	Bader charge/e	CO adsorption energy/eV
$\text{B}_O$	+0.55	−2.54
$\text{O}_V$	−0.29	+0.05
$\text{O}_V\text{-O}_2$	+1	−1.68

reflected in the significantly higher integrated density, indicative of greater electron density, consistent with earlier Bader charge and valence state analyses. Conversely, the valence electrons of the Au atoms in the other two configurations ( $\text{O}_V$  and  $\text{O}_V\text{-O}_2$ ) are closer to the Fermi level, indicating higher energy and reactivity, therefore a greater likelihood of interacting with other atoms. As a result, the  $\text{Au}^{\delta+}$  in these configurations is catalytically active for CO activation. The Bader charges and CO adsorption energies for Au atoms on these different structures are collected in Table 1.

The valence changes of the Au atom in the  $\text{Au}_1@ \text{CeO}_2(111)$  catalyst, which lead to catalyst deactivation and reactivation, are crucial for understanding the CO oxidation mechanisms on this catalyst. As shown in Fig. 4, the CO oxidation mechanisms include three steps: (I) initial CO oxidation on stoichiometric  $\text{Au}_1@ \text{CeO}_2(111)$ , resulting in the formation of an oxygen vacancy and  $\text{CO}_2$  release (Fig. 4(a)), (II) molecular  $\text{O}_2$  adsorption at the vacancy, leading to the formation of surface oxygen species (Fig. 4(b)), and (III) interaction of another CO molecule with these oxygen species, driving the formation of the second  $\text{CO}_2$  molecule (Fig. 4(c)) and regenerating the catalyst. The rate-limiting step occurs when the second adsorbed CO molecule reacts with surface oxygen species, requiring an activation energy of just 0.55 eV (Fig. 4j and k), highlighting the high activity of the  $\text{Au}_1@ \text{CeO}_2(111)$  catalyst toward CO oxidation. Throughout these processes, the Au atom oscillates between negative and positive oxidation states, where negative states contribute to high stability and positive states contribute to high activity. Under the CO reaction conditions, the Au atoms can adaptively change their oxidation states in response to the adsorbed species to achieve both high stability and activity simultaneously.

### Thermodynamic analysis of Au valence states and oxygen vacancy formation under reaction conditions

To comprehensively address the environmental adaptability of the  $\text{Au}_1@ \text{CeO}_2(111)$  catalyst, we performed *ab initio* thermodynamic analyses to systematically investigate the effects of reaction temperature and partial pressures of CO and  $\text{CO}_2$  on the valence state of Au single atoms and the formation of oxygen vacancies on the  $\text{CeO}_2(111)$  surface (Fig. 5). Specifically, we analysed two distinct pathways for the transition from the initial structure (Fig. 4a) to the oxygen vacancy-containing structure (Fig. 4f), where the Au atom shifts from a positively charged ( $\text{Au}^{\delta+}$ ) state to a negatively charged ( $\text{Au}^{\delta-}$ ) state.

Pathway I corresponds to the CO oxidation process (Fig. 4a–f), where CO reacts with lattice oxygen to form  $\text{CO}_2$  and generate an oxygen vacancy. Pathway II involves the direct formation of an oxygen vacancy without CO oxidation. For pathway I, the Gibbs free energy change ( $\Delta G$ ) was calculated under varying CO and  $\text{CO}_2$

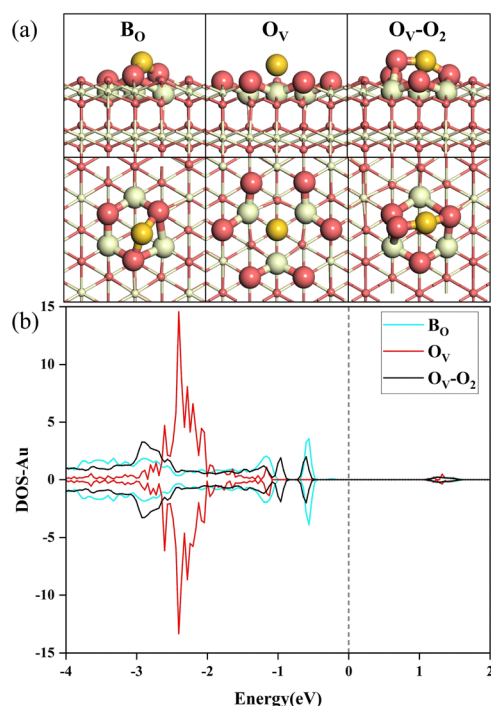


**Fig. 3** (a) Configuration of  $\text{B}_O$ ,  $\text{O}_V$  and  $\text{O}_V\text{-O}_2$ . (b) Density of states (DOS) for Au atom adsorption at various sites including the bridge site of surface oxygen ( $\text{B}_O$ ), the top site of the surface oxygen vacancy ( $\text{O}_V$ ), and the site with the oxygen vacancy filled by an  $\text{O}_2$  molecule ( $\text{O}_V\text{-O}_2$ ).



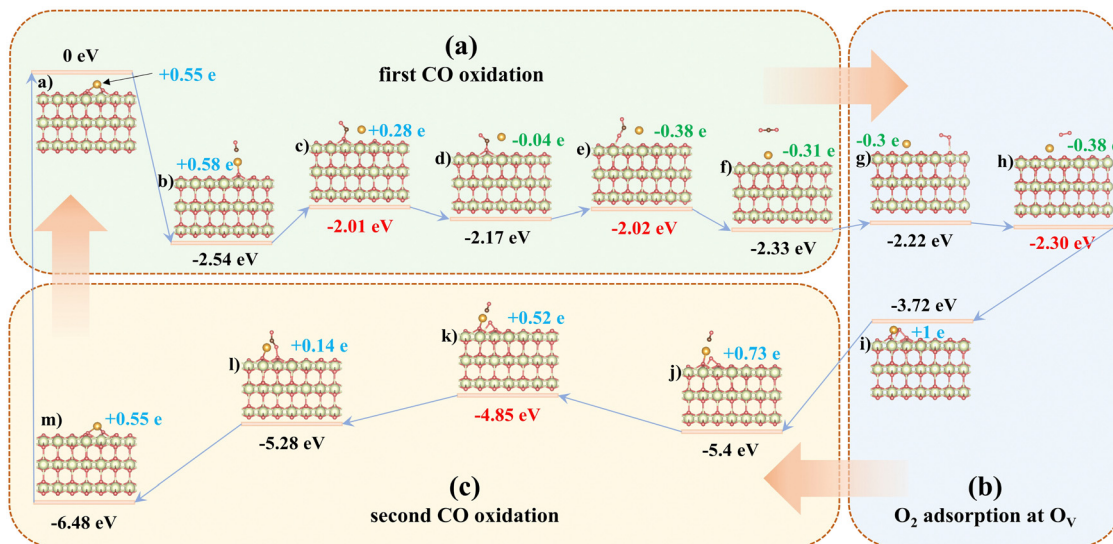


Fig. 4 Computed reaction pathway diagram of  $\text{Au}_1@ \text{CeO}_2(111)$  catalyzed CO oxidation. (a) First CO oxidation, (b)  $\text{O}_2$  adsorption at  $\text{O}_v$ , and (c) second CO oxidation. The structure represented by the red number is the transition state configuration.

partial pressures at three representative temperatures: 574 K, 874 K, and 1174 K (Fig. 5a–c). At 574 K, the  $\Delta G = 0$  contour intersects at CO partial pressures of  $\sim 1 \times 10^{-16}$  mbar ( $\text{CO}_2$ :  $\sim 1 \times 10^4$  mbar) and  $\sim 1 \times 10^{-2}$  mbar ( $\text{CO}_2$ :  $\sim 1 \times 10^{18}$  mbar), indicating that higher CO pressures and lower  $\text{CO}_2$  pressures thermodynamically favour the reaction ( $\Delta G < 0$ ). As the temperature increases to 874 K and 1174 K, the  $\Delta G = 0$  contour shifts toward lower  $\text{CO}_2$  pressures, demonstrating enhanced spontaneity of oxygen vacancy formation at elevated temperatures.

For pathway II (direct oxygen vacancy generation, Fig. 5d), the reaction is endothermic ( $\Delta E = 1.13$  eV) with  $\text{O}_2$  as a product. The equilibrium condition ( $\Delta G = 0$ ) requires extremely low  $\text{O}_2$  partial pressures ( $< 1 \times 10^{-16}$  mbar) at temperatures above 400 K, while at higher  $\text{O}_2$  pressures (e.g.,  $1 \times 10^4$  mbar), temperatures exceeding 1274 K are needed to drive the reaction. This stark contrast highlights the critical role of CO oxidation (pathway I) in facilitating oxygen vacancy formation under experimentally relevant conditions.

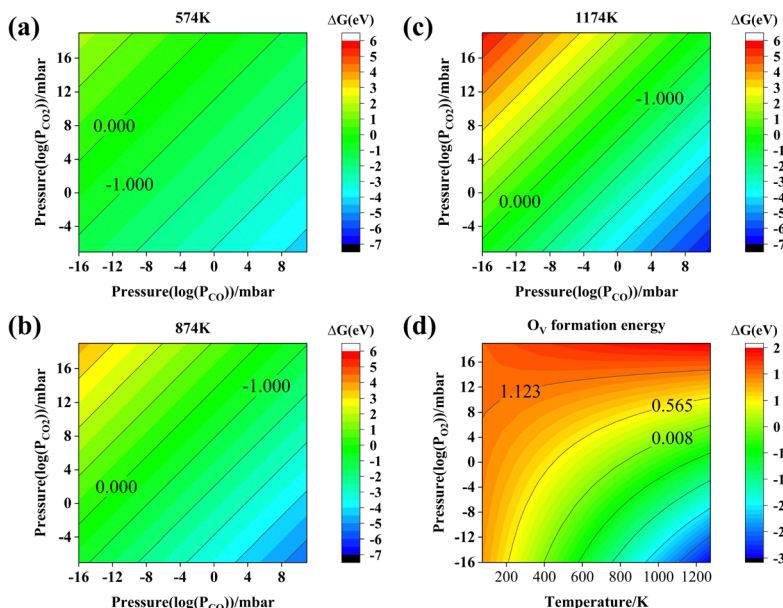


Fig. 5 Thermodynamic analysis of the  $\text{Au}_1@ \text{CeO}_2(111)$  catalyst under varying environmental conditions. (a) Gibbs free energy change ( $\Delta G$ ) for CO oxidation (pathway I) at 574 K as a function of CO and  $\text{CO}_2$  partial pressures. (b)  $\Delta G$  profiles for pathway I at 874 K, illustrating the shift of the equilibrium toward lower  $\text{CO}_2$  pressures. (c)  $\Delta G$  analysis at 1174 K, highlighting enhanced spontaneity of oxygen vacancy formation at elevated temperatures. (d) Thermodynamic equilibrium ( $\Delta G = 0$ ) for direct oxygen vacancy generation (pathway II), plotted against temperature and  $\text{O}_2$  partial pressure. All contours correspond to calculated free energy landscapes.



These thermodynamic insights elucidate how environmental parameters (temperatures and gas pressures) dynamically regulate the valence state of Au atoms and oxygen vacancy populations on the CeO<sub>2</sub>(111) surface. The adaptive switching between Au<sup>δ+</sup> and Au<sup>δ−</sup> states, coupled with the temperature- and pressure-dependent vacancy formation, underpins the dual stability and activity of the Au<sub>1</sub>@CeO<sub>2</sub>(111) catalyst during CO oxidation.

### Valence state oscillations of the supported gold cluster catalysts under CO oxidation reaction conditions

To elucidate the unique properties of the Au<sub>1</sub>@CeO<sub>2</sub>(111) catalyst, we analyzed the CO oxidation processes in the Au<sub>4</sub>@CeO<sub>2</sub>(111) and Au<sub>10</sub>@CeO<sub>2</sub>(111) catalysts (Fig. S9–S11 and Tables S1, S2, ESI†). The stable configurations of Au<sub>4</sub> and Au<sub>10</sub> clusters on CeO<sub>2</sub>(111) were referenced from Zhang *et al.*'s literature,<sup>36</sup> and the structure search method was not used to determine the structure of Au clusters. Bader charge analysis throughout the reaction processes showed that the charge changes in gold atoms for Au<sub>4</sub>@CeO<sub>2</sub>(111) and Au<sub>10</sub>@CeO<sub>2</sub>(111) are less significant compared to those in Au<sub>1</sub>@CeO<sub>2</sub>(111). This indicates that valence state oscillations are more pronounced in Au<sub>1</sub>@CeO<sub>2</sub>(111), while in the larger clusters of Au<sub>4</sub>@CeO<sub>2</sub>(111) and Au<sub>10</sub>@CeO<sub>2</sub>(111), the changes are less significant and distributed among all gold atoms in the cluster, resulting in less noticeable shifts per atom. This non-adaptive behavior with respect to environmental changes has less impact on the catalytic activity of these larger gold clusters during CO oxidation. Consequently, the reaction barriers are higher for Au<sub>4</sub>@CeO<sub>2</sub>(111) and Au<sub>10</sub>@CeO<sub>2</sub>(111), at 1.59 eV and 0.82 eV, respectively, compared to 0.55 eV for Au<sub>1</sub>@CeO<sub>2</sub>(111). In contrast, the Au<sub>1</sub>@CeO<sub>2</sub>(111) catalyst can effectively oscillate its valence state between positive and negative under varying atmospheric conditions, adapting its valence to suit different reaction environments and maintaining high activity and stability throughout the CO oxidation process.

## Conclusions

This study provides a comprehensive analysis of the catalytic activity and mechanisms of CO oxidation on Au<sub>1</sub>@CeO<sub>2</sub>(111) catalysts, using DFT+*U* calculations, and compares these results with those obtained for Au<sub>4</sub>@CeO<sub>2</sub>(111) and Au<sub>10</sub>@CeO<sub>2</sub>(111) catalysts. Our findings highlight the crucial role of the valence state of the Au atom in influencing the performance of the catalyst. In a CO atmosphere, CO reacts with surface lattice oxygen to form an oxygen vacancy, stabilizing the Au atom in a catalytically inactive Au<sup>δ−</sup> state. In an O<sub>2</sub> atmosphere, the deactivated Au atom is reactivated by molecular oxygen filling the oxygen vacancy, converting the Au<sup>δ−</sup> state to a catalytically active Au<sup>δ+</sup> state. The detailed electronic structure analysis, including density of states calculations and Bader charge analysis, confirms that the Au<sup>δ−</sup> state is electronically stable, while the Au<sup>δ+</sup> state is active and essential for CO oxidation. Unlike Au<sub>4</sub>@CeO<sub>2</sub>(111) and Au<sub>10</sub>@CeO<sub>2</sub>(111) catalysts, where the Au valence state is less responsive to environmental changes, the Au<sub>1</sub>@CeO<sub>2</sub>(111) catalyst

effectively adjusts its valence state during the reaction, maintaining both high activity and stability for CO oxidation. This study advances the fundamental understanding of the unique properties of single-atom catalysis and paves the way for practical manipulation of single-atom catalyst behaviors.

## Data availability

The data supporting this article have been included as part of the ESI.†

## Conflicts of interest

There are no conflicts to declare.

## Acknowledgements

We acknowledge the financial support from the National Key Research and Development Program of China (2022YFA1505500 and 2023YFA1506904), the National Natural Science Foundation of China (22302173, 52025011, 92045301, 51971202, and 52171019), and the Fundamental Research Funds for the Central Universities.

## Notes and references

- 1 B. Qiao, A. Wang, X. Yang, L. F. Allard, Z. Jiang, Y. Cui, J. Liu, J. Li and T. Zhang, *Nat. Chem.*, 2011, **3**, 634–641.
- 2 H. He, H. H. Wang, J. Liu, X. Liu, W. Li and Y. Wang, *Molecules*, 2021, **26**, 6501.
- 3 B. Han, T. Li, J. Zhang, C. Zeng, H. Matsumoto, Y. Su, B. Qiao and T. Zhang, *Chem. Commun.*, 2020, **56**, 4870–4873.
- 4 F. Li, Y. Li, X. C. Zeng and Z. Chen, *ACS Catal.*, 2015, **5**, 544–552.
- 5 Y. Lu, J. Wang, L. Yu, L. Kovarik, X. Zhang, A. S. Hoffman, A. Gallo, S. R. Bare, D. Sokaras, T. Kroll, V. Dagle, H. Xin and A. M. Karim, *Nat. Catal.*, 2018, **2**, 149–156.
- 6 B. Qiao, J.-X. Liang, A. Wang, J. Liu and T. Zhang, *Chin. J. Catal.*, 2016, **37**, 1580–1586.
- 7 J. Xu, Y. Wang, K. Wang, M. Zhao, R. Zhang, W. Cui, L. Liu, M. S. Bootharaju, J. H. Kim, T. Hyeon, H. Zhang, Y. Wang, S. Song and X. Wang, *Angew. Chem., Int. Ed.*, 2023, **62**, e202302877.
- 8 B.-H. Lee, E. Gong, M. Kim, S. Park, H. R. Kim, J. Lee, E. Jung, C. W. Lee, J. Bok, Y. Jung, Y. S. Kim, K.-S. Lee, S.-P. Cho, J.-W. Jung, C.-H. Cho, S. Lebegue, K. T. Nam, H. Kim, S.-I. In and T. Hyeon, *Energy Environ. Sci.*, 2022, **15**, 601–609.
- 9 Y. Zhu, S. F. Yuk, J. Zheng, M.-T. Nguyen, M.-S. Lee, J. Szanyi, L. Kovarik, Z. Zhu, M. Balasubramanian, V.-A. Glezakou, J. L. Fulton, J. A. Lercher, R. Rousseau and O. Y. Gutiérrez, *J. Am. Chem. Soc.*, 2021, **143**, 5540–5549.
- 10 S. Chen, B. Wang, J. Zhu, L. Wang, H. Ou, Z. Zhang, X. Liang, L. Zheng, L. Zhou, Y.-Q. Su, D. Wang and Y. Li, *Nano Lett.*, 2021, **21**, 7325–7331.





- 11 Y. Guo, S. Mei, K. Yuan, D.-J. Wang, H.-C. Liu, C.-H. Yan and Y.-W. Zhang, *ACS Catal.*, 2018, **8**, 6203–6215.
- 12 M.-M. Millet, G. Algara-Siller, S. Wrabetz, A. Mazheika, F. Girgsdies, D. Teschner, F. Seitz, A. Tarasov, S. V. Levchenko, R. Schlögl and E. Frei, *J. Am. Chem. Soc.*, 2019, **141**, 2451–2461.
- 13 B. Han, X. Ou, Z. Deng, Y. Song, C. Tian, H. Deng, Y. Xu and Z. Lin, *Angew. Chem., Int. Ed.*, 2018, **130**, 17053–17057.
- 14 F. J. Caparrós, L. Soler, M. D. Rossell, I. Angurell, L. Piccolo, O. Rossell and J. Llorca, *ChemCatChem*, 2018, **10**, 2365–2369.
- 15 B. Wu, X. Yu, M. Huang, L. Zhong and Y. Sun, *Chin. J. Chem. Eng.*, 2022, **43**, 62–69.
- 16 Y. Wang, H. Arandiyán, J. Scott, K.-F. Aguey-Zinsou and R. Amal, *ACS Appl. Energy Mater.*, 2018, **1**, 6781–6789.
- 17 S. Dong, W. Liu, S. Liu, F. Li, J. Hou, R. Hao, X. Bai, H. Zhao, J. Liu and L. Guo, *Mater. Today Nano*, 2022, **17**, 100157.
- 18 Y. Wang, Z. Chen, P. Han, Y. Du, Z. Gu, X. Xu and G. Zheng, *ACS Catal.*, 2018, **8**, 7113–7119.
- 19 J. Liang, J. Lin, J. Liu, X. Wang, T. Zhang and J. Li, *Angew. Chem., Int. Ed.*, 2020, **59**, 12868–12875.
- 20 X. Chen, C. Qu, Y. Xiao, W. Wang, J. Zhang, X. Zheng and Q. Ye, *Catal. Today*, 2024, **434**, 114687.
- 21 X. Sun, J. Lin, Y. Zhou, L. Li, Y. Su, X. Wang and T. Zhang, *AIChE J.*, 2017, **63**, 4022–4031.
- 22 L. Sun, J. Xu, X. Liu, B. Qiao, L. Li, Y. Ren, Q. Wan, J. Lin, S. Lin, X. Wang, H. Guo and T. Zhang, *ACS Catal.*, 2021, **11**, 5942–5950.
- 23 J. Lin, A. Wang, B. Qiao, X. Liu, X. Yang, X. Wang, J. Liang, J. Li, J. Liu and T. Zhang, *J. Am. Chem. Soc.*, 2013, **135**, 15314–15317.
- 24 L. Sun, L. Cao, Y. Su, C. Wang, J. Lin and X. Wang, *Appl. Catal., B*, 2022, **318**, 121841.
- 25 Y. Li, Z. Zhao, W. Lu, H. Zhu, F. Sun, B. Mei, Z. Jiang, Y. Lyu, X. Chen, L. Guo, T. Wu, X. Ma, Y. Meng and Y. Ding, *Appl. Catal., B*, 2023, **324**, 122298.
- 26 W. Zhang, A. Vidal-López and A. Comas-Vives, *Front. Chem.*, 2023, **11**, 1144189.
- 27 J. Li, L. Sun, Q. Wan, J. Lin, S. Lin and X. Wang, *J. Phys. Chem. Lett.*, 2021, **12**, 11415–11421.
- 28 P. Liu, Y. Zhao, R. Qin, S. Mo, G. Chen, L. Gu, D. M. Chevrier, P. Zhang, Q. Guo, D. Zang, B. Wu, G. Fu and N. Zheng, *Science*, 2016, **352**, 797–800.
- 29 X. Xie, C. He, B. Li, Y. He, D. A. Cullen, E. C. Wegener, A. J. Kropf, U. Martinez, Y. Cheng, M. H. Engelhard, M. E. Bowden, M. Song, T. Lemmon, X. S. Li, Z. Nie, J. Liu, D. J. Myers, P. Zelenay, G. Wang, G. Wu, V. Ramani and Y. Shao, *Nat. Catal.*, 2020, **3**, 1044–1054.
- 30 G. Kyriakou, M. B. Boucher, A. D. Jewell, E. A. Lewis, T. J. Lawton, A. E. Baber, H. L. Tierney, M. Flytzani-Stephanopoulos and E. C. H. Sykes, *Science*, 2012, **335**, 1209–1212.
- 31 M. Tong, F. Sun, Y. Xie, Y. Wang, Y. Yang, C. Tian, L. Wang and H. Fu, *Angew. Chem., Int. Ed.*, 2021, **60**, 14005–14012.
- 32 C. Riley, S. Zhou, D. Kunwar, A. De La Riva, E. Peterson, R. Payne, L. Gao, S. Lin, H. Guo and A. Datye, *J. Am. Chem. Soc.*, 2018, **140**, 12964–12973.
- 33 M. F. Camellone and S. Fabris, *J. Am. Chem. Soc.*, 2009, **131**, 10473–10483.
- 34 Z. Guo, J. Zhang, Y. Luo, D. Li, R. Zhao, Y. Huang, H. Ren and X. Yao, *Nanotechnology*, 2023, **34**, 285101.
- 35 C. Zhang, A. Michaelides, D. A. King and S. J. Jenkins, *J. Phys. Chem. C*, 2009, **113**, 6411–6417.
- 36 C. Zhang, A. Michaelides, D. A. King and S. J. Jenkins, *J. Am. Chem. Soc.*, 2010, **132**, 2175–2182.
- 37 P. E. Blöchl, *Phys. Rev. B: Condens. Matter Mater. Phys.*, 1994, **50**, 17953–17979.
- 38 G. Kresse and J. Furthmüller, *Phys. Rev. B: Condens. Matter Mater. Phys.*, 1996, **54**, 11169–11186.
- 39 J. P. Perdew, K. Burke and M. Ernzerhof, *Phys. Rev. Lett.*, 1996, **77**, 3865–3868.
- 40 S. L. Dudarev, G. A. Botton, S. Y. Savrasov, C. J. Humphreys and A. P. Sutton, *Phys. Rev. B: Condens. Matter Mater. Phys.*, 1998, **57**, 1505–1509.
- 41 M. Cococcioni and S. De Gironcoli, *Phys. Rev. B: Condens. Matter Mater. Phys.*, 2005, **71**, 035105.
- 42 M. Nolan, S. Grigoleit, D. C. Sayle, S. C. Parker and G. W. Watson, *Surf. Sci.*, 2005, **576**, 217–229.
- 43 C. W. M. Castleton, J. Kullgren and K. Hermansson, *J. Chem. Phys.*, 2007, **127**, 244704.
- 44 G. Kresse and D. Joubert, *Phys. Rev. B: Condens. Matter Mater. Phys.*, 1999, **59**, 1758–1775.
- 45 G. Henkelman, B. P. Uberuaga and H. Jónsson, *J. Chem. Phys.*, 2000, **113**, 9901–9904.
- 46 H. Jónsson, G. Mills and K. W. Jacobsen, *Classical and Quantum Dynamics in Condensed Phase Simulations*, World Scientific, 1998, pp. 385–404.
- 47 G. Henkelman and H. Jónsson, *J. Chem. Phys.*, 1999, **111**, 7010–7022.

